
LOADING AND RELAXATION DYNAMICS OF A RED BLOOD CELL \dagger

Fabio Guglietta

Department of Physics & INFN, University of Rome “Tor Vergata”*

Chair for Computational Analysis of Technical Systems (CATS), RWTH Aachen University †

Computation-based Science and Technology Research Center, The Cyprus Institute ‡

fabio.guglietta@roma2.infn.it

Marek Behr

Chair for Computational Analysis of Technical Systems (CATS), RWTH Aachen University †

Giacomo Falcucci

Department of Enterprise Engineering “Mario Lucertini,” University of Rome “Tor Vergata” §

Mauro Sbragaglia

Department of Physics & INFN, University of Rome “Tor Vergata”*

ABSTRACT

We use mesoscale numerical simulations to investigate the unsteady dynamics of a single red blood cell (RBC) subject to an external mechanical load. We carry out a detailed comparison between the *loading* (L) dynamics, following the imposition of the mechanical load on the RBC at rest, and the *relaxation* (R) dynamics, allowing the RBC to relax to its original shape after the sudden arrest of the mechanical load. Such comparison is carried out by analyzing the characteristic times of the two corresponding dynamics, i.e., t_L and t_R . For small intensities of the mechanical load, the two dynamics are *symmetrical* ($t_L \approx t_R$) and independent on the typology of mechanical load (intrinsic dynamics); in marked contrast, for finite intensities of the mechanical load, an *asymmetry* is found, wherein the loading dynamics is typically faster than the relaxation one. This asymmetry manifests itself with non-universal characteristics, e.g., dependency on the applied load and/or on the viscoelastic properties of the RBC membrane. To deepen such a non-universal behaviour, we consider the viscosity of the erythrocyte membrane as a variable parameter and focus on three different typologies of mechanical load (mechanical stretching, shear flow, elongational flow): this allows to clarify how non-universality builds-up in terms of the deformation and rotational contributions induced by the mechanical load on the membrane. Our results provide crucial and quantitative information on the unsteady dynamics of RBC and on its membrane response to the imposition/cessation of external mechanical loads.

1 Introduction

Red blood cells (RBCs) are biological cells made of a viscoelastic membrane enclosing a viscous fluid (cytoplasm): their main features are the biconcave shape and the absence

of a nucleus and most organelles, that allow them to carry oxygen even inside the smallest capillaries [1, 2, 3]. In fact, during the circulation, RBCs deform multiple times, rearranging their shape to adapt to the physiological conditions of the blood flow. The mechanical properties of RBC’s membrane have been deeply investigated, both numerically [3, 4, 5, 6, 7, 8, 9, 10, 11, 12, 13, 14] and experimentally [15, 16, 17, 18, 19, 20, 21, 22, 23]. Research interest on the mechanical response of RBC’s

\dagger Electronic Supplementary Information (ESI) and four videos showing the simulations performed are available in the Ancillary Files. A brief description of the movies is provided in ESI.

membrane was prompted by several reasons: among the others, the link between its properties and the erythrocyte's health conditions [11, 16], or the role played by the membrane dynamics in the design of biomedical devices[24, 25, 26, 27]. A huge effort has been devoted to the characterization of the time-independent properties of the membrane, towards the definition of the corresponding steady-state configurations. In recent years, also the dynamical behaviour of RBCs has been investigated in several works, both numerically [28, 29, 30, 31, 8, 32, 33, 34] and experimentally [17, 19, 20, 35]. When dealing with time-dependent properties of biological cells (or capsules, in general), the membrane viscosity plays a crucial role [36, 37, 38, 33, 34, 39, 40, 41, 42, 43]. Evans [44] showed that the RBC relaxation time is affected by both the membrane viscosity and the dissipation in the adjacent aqueous phases (i.e., cytoplasm and external solution); neglecting the membrane viscosity, i.e., $\mu_m = 0$, he predicted a relaxation time $t_R \approx 1 \times 10^{-3}$ s (also confirmed by numerical simulations [33]), a remarkably lower value compared to other works in the literature [22, 19, 17, 45, 33]. Several works aimed at the precise estimation of the value of the membrane viscosity [46, 18, 45, 47, 22, 48, 49, 17, 19, 32], finding that μ_m roughly ranges between 10^{-7} m Pa s and 10^{-6} m Pa s. Such a variability may be ascribed to different factors, e.g., the different theoretical models used to infer μ_m [19, 46], the different experimental apparatuses (such as micro-pipette aspiration [46, 18, 45, 17], microchannel deformation [49], or other setups [47, 22, 48]), etc. As a matter of fact, although μ_m is an essential parameter to quantitatively characterize the time dynamics of RBCs [34, 37], its precise value has not been accurately determined so far, which warrants a parametric investigation. Moreover, some earlier studies [50] proposed to use an increased apparent viscosity ratio to account for the energy dissipation due to the presence of a viscous membrane: even though this assumption provides a qualitative description of the effects due to the presence of the membrane viscosity, it does not account for a quantitative characterisation, as shown by recent studies [37, 34, 41, 40]. Our previous work [33] aimed to investigate the effect of membrane viscosity μ_m on the relaxation dynamics of a single RBC, and we found that increasing the value of μ_m , as well as increasing the intensity of the loading strength, leads to a fast recovery dynamics. Moreover, we simulated two experimental setups, i.e., the stretching with optical tweezers and the deformation due to an imposed shear flow, and we found a dependency on the kind of mechanical load for finite strengths of the load.

The relaxation dynamics, however, gives only a partial characterization of the time-dependent response of RBCs to external forces. Obviously, the loading process should be considered, as well, as already pointed out in earlier literature papers. Chien *et al.* [18] experimentally studied both the loading and the relaxation dynamics of RBC membrane through micro-pipette aspiration, providing evidence that the two dynamics are not symmetrical

in certain conditions; however, a systematic study involving different stress values and different typologies of mechanical loads was not performed. Diaz *et al.* [43] studied the dynamics of a pure elastic capsule with a hyperelastic membrane deformed by an elongational flow: they focused on both loading and relaxation, finding an asymmetry. However, their model did not take into account the membrane viscosity and the asymmetry was not studied for different typologies of mechanical loads. Thus, although previous literature points to two distinct dynamics for loading and relaxation [18, 43, 42], a comprehensive parametric study on the effects of μ_m for different typologies of mechanical loads and flow conditions (such as simple shear flow or elongational flow) has never been attempted, so far. This paper aims at filling this gap with the help of mesoscale numerical simulations. Indeed, for this kind of characterization, numerical simulations can be thought of as the appropriate tool of analysis [3, 4, 5, 6, 7, 8, 9, 10, 11, 12, 13, 14], due to the obvious experimental difficulties in carrying out such systematic investigation [17, 18, 19, 21, 23]. We provide a quantitative characterisation of loading and relaxation dynamics exploring three typologies of mechanical loads. To do this, we built three different simulation setups: the stretching simulation (STS), which simulates the deformation with optical tweezers [16] (see Fig. 1, panel (a)); the shear simulation (SHS), i.e., the deformation in simple shear flow (see Fig. 1, panel (c)); the four-roll mill simulation (FRMS), where the deformation is induced by an elongational axisymmetric flow made by the rotation of four cylinders (see Fig. 1, panel (e)). These three numerical setups are chosen to inspect the different roles that the membrane rotation and/or membrane deformation have in the time-dependent dynamics. This information is summarised in Tab. 1. We systematically study the characteristic times of both the loading (t_L) and the relaxation (t_R) processes and their ratio $t = t_L/t_R$, as a function of the load strength and membrane viscosity μ_m . For small strengths, the two characteristic times are essentially equal and set by the value of μ_m ; however, for finite strengths, the loading dynamics is found to be faster than the relaxation dynamics, leading to a non-universal behaviour while changing the typology of the mechanical load. Such non-universal contributions are further characterized in terms of the importance of rotation and deformation of the membrane, according to the different load mechanisms. Some useful parametrizations for both t_R and t_L as a function of the membrane viscosities are also provided. The paper is organised in the following way: in Sec. 2 we provide some details on the numerical method used to simulate both the fluid and the membrane of the RBC; in Sec. 3 we analyse the three simulated loading mechanisms (the stretching simulation, Sec. 3.1; the shear simulation, Sec. 3.2; the four-roll mill simulation, Sec. 3.3); a detailed discussion section with comparisons between the loading mechanisms is provided in Sec. 4; finally, conclusions are reported in Sec. 5.

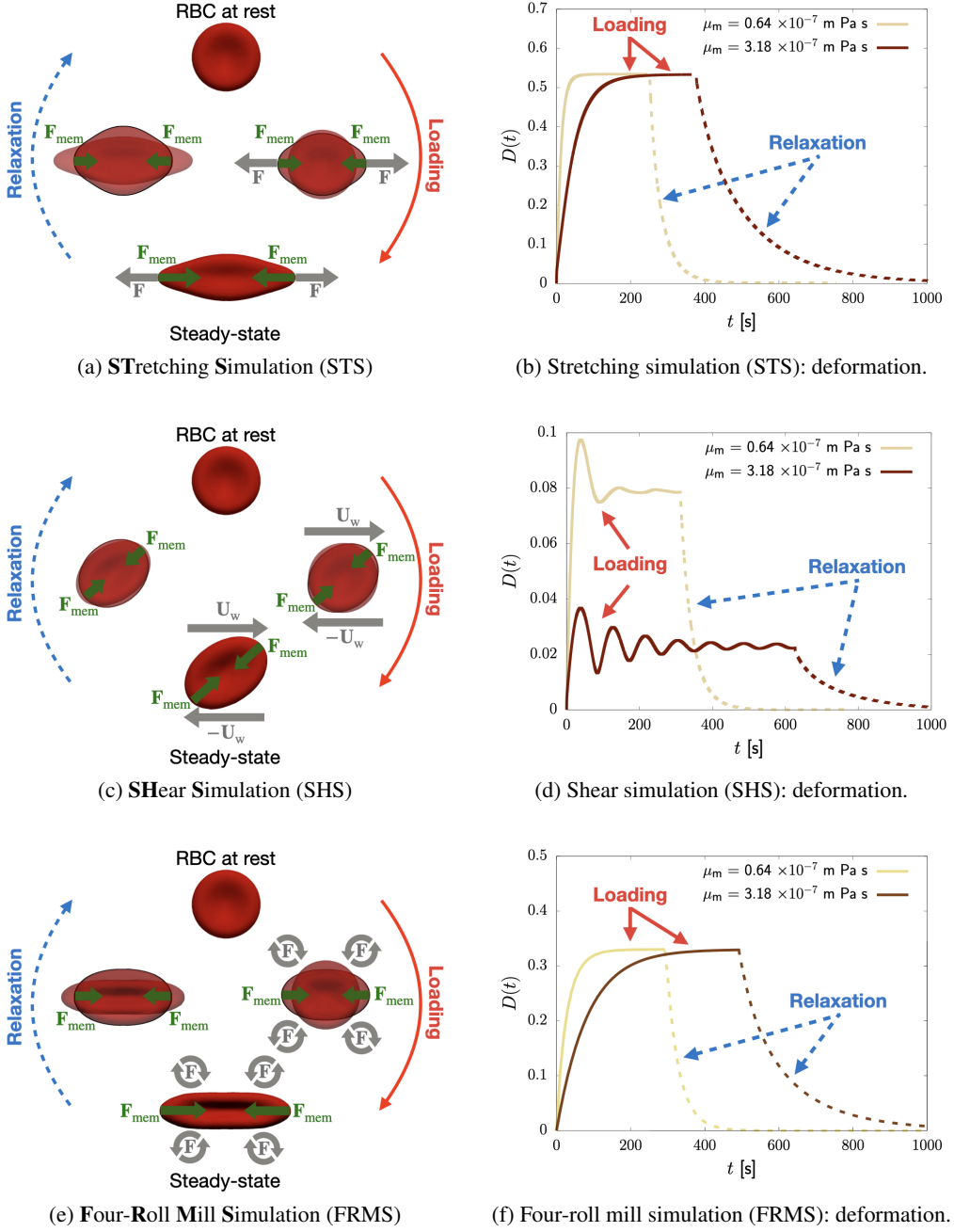


Figure 1: Loading-relaxation (L-R) experiments for red blood cell (RBC) at changing the typology of mechanical load. *Left panels*: the three different L-R experiments investigated in the paper are sketched: grey arrows refer to the mechanical load, either an applied force \mathbf{F} or an applied velocity \mathbf{U}_w , while the RBC membrane forces (\mathbf{F}_{mem}) are sketched with green arrows. In all simulation, the deformation $D(t)$, i.e., the ratio between the difference and the sum of the two longest diameters (see Eq. 11), is used to fit the loading and relaxation times (t_L and t_R , respectively; see Eqs. (12) (13) (14)). *Right panels*: we report the deformation $D(t)$ (see Eq. (11)) as a function of time for two values of membrane viscosity μ_m . *Panels (a-b)*: we simulate the stretching with optical tweezers [16] (STS), in which two forces with the same intensity and opposite direction stretch the membrane in two areas at the end of the RBC (see Sec. 3.1); the deformation $D(t)$ is reported for $F = 90 \times 10^{-12} \text{ N}$. *Panels (c-d)*: deformation induced by simple shear flow (SHS), with $\mathbf{U}_w = (\pm \dot{\gamma}/2, 0, 0)$, where $\dot{\gamma}$ is the shear rate (see Sec. 3.2); the deformation $D(t)$ is reported for $\dot{\gamma} = 86 \text{ s}^{-1}$. *Panels (e-f)*: in the four-roll mill simulation (FRMS) we simulate four rotating cylinders to reproduce an elongational flow that deforms the membrane [51] (see Sec. 3.3); the deformation $D(t)$ is reported for $F_{\text{roll}} = 80 \text{ s}^{-1}$. Four videos showing these simulations are available (see Ancillary Files†).

Load Type	Rotation	Direct Forcing
STS	NO	YES
SHS	YES	NO
FRMS	NO	NO

Table 1: Summary of the main characteristics of the three kinds of applied mechanical load (see Fig. 1). For each load type, we specify if the rotation is induced on the membrane while loading and if the forcing is directly applied on the nodes of the mesh used to discretise the membrane (otherwise, the membrane is forced indirectly via hydrodynamic flow).

2 Numerical method

We perform three-dimensional numerical simulations in the framework of the Immersed Boundary – Lattice Boltzmann method (IB–LBM) [52, 53]. The methodology, as well as the membrane model, are the same already used and validated in [33]: here we report an essential summary. The equation of motion for a fluid with viscosity μ is given by Navier-Stokes (NS) equation

$$\rho \left(\frac{\partial \mathbf{u}}{\partial t} + (\mathbf{u} \cdot \nabla) \mathbf{u} \right) = -\nabla p + \mu \nabla^2 \mathbf{u} + \mathbf{F}, \quad (1)$$

where ρ and \mathbf{u} are the density and the velocity of the fluid, respectively; p is the isotropic pressure; \mathbf{F} is an external body force. If the fluid is incompressible (as in the present work) the condition $\nabla \cdot \mathbf{u} = 0$ holds.

In the LBM, instead of directly solving NS equation by integrating Eq. (1), the fluid is represented by the so-called populations $f_i(\mathbf{x}, t)$, that stand for the density of fluid molecules moving with velocity \mathbf{c}_i at position \mathbf{x} and time t . The populations evolve according to the Lattice Boltzmann equation:

$$\begin{aligned} f_i(\mathbf{x} + \mathbf{c}_i \Delta t, t + \Delta t) - f_i(\mathbf{x}, t) &= \\ = -\frac{\Delta t}{\tau} \left(f_i(\mathbf{x}, t) - f_i^{(\text{eq})}(\mathbf{x}, t) \right) + f_i^{(F)}, \end{aligned} \quad (2)$$

in which Δt is the discrete time step, τ is the relaxation time, $f_i^{(F)}$ is the source term which takes into account the force density (it has been implemented according to the “Guo” scheme [54]), and $f_i^{(\text{eq})}$ is the equilibrium distribution function (we refer back to [52, 53] for the details). The fluid density ρ and the velocity \mathbf{u} are given by:

$$\begin{aligned} \rho(\mathbf{x}, t) &= \sum_i f_i(\mathbf{x}, t), \\ \rho \mathbf{u}(\mathbf{x}, t) &= \sum_i \mathbf{c}_i f_i(\mathbf{x}, t). \end{aligned} \quad (3)$$

The link between NS and LB equations (Eq. (1) and Eq. (2), respectively) is given by the following relation:

$$\mu = \rho c_s^2 \left(\tau - \frac{\Delta t}{2} \right), \quad (4)$$

where $c_s = \Delta x / \Delta t \sqrt{3}$ is the speed of sound. In the following, we considered both the lattice spacing Δx and the time interval Δt equal to 1.

We simulate two fluids: one outside the membrane (the plasma, with viscosity $\mu_{\text{out}} = 1.2 \times 10^{-3}$ Pa s) and one inside it (the cytosol, with viscosity $\mu_{\text{in}} = 6 \times 10^{-3}$ Pa s). The viscosity ratio is given by

$$\lambda = \frac{\mu_{\text{in}}}{\mu_{\text{out}}}, \quad (5)$$

providing $\lambda = 5$. We implemented the parallel Hoshen-Kopelman algorithm to recognise which lattice sites are inside or outside the membrane (see [55] for details).

The RBC membrane is described as a 3D triangular mesh of ≈ 4000 elements, whose shape at rest is given by [56]

$$\begin{aligned} z(x, y) = \pm \sqrt{1 - \frac{x^2 + y^2}{r^2}} \cdot \\ \cdot \left(C_0 + C_1 \frac{x^2 + y^2}{r^2} + C_2 \left(\frac{x^2 + y^2}{r^2} \right)^2 \right), \end{aligned} \quad (6)$$

with $C_0 = 0.81 \times 10^{-6}$ m, $C_1 = 7.83 \times 10^{-6}$ m and $C_2 = -4.39 \times 10^{-6}$ m; $r = 3.91 \times 10^{-6}$ m is the large radius.

The membrane is characterised by a resistance to shear deformation, area dilation and bending; the viscoelastic behaviour is implemented, as well. The first two terms form the strain energy W_S are described by Skalak model [57]:

$$W_S = \sum_j A_j \left[\frac{k_S}{8} (I_1^2 + 2I_1 - 2I_2) + \frac{k_\alpha}{8} I_2^2 \right], \quad (7)$$

where $k_S = 5.3 \times 10^{-6}$ N m⁻¹ [16] and $k_\alpha = 50k_S$ [3] are the surface elastic shear modulus and the area dilation modulus, respectively; $I_1 = \lambda_1^2 + \lambda_2^2 - 2$ and $I_2 = \lambda_1^2 \lambda_2^2 - 1$ are the strain invariants for the j -th element, while λ_1 and λ_2 are the principal stretch ratios [57, 3]. We adopt the Helfrich formulation to compute the free-energy W_B related to the resistance to bending [58]. Following [3], we discretise the bending energy as:

$$W_B = \frac{k_B \sqrt{3}}{2} \sum_{\langle i,j \rangle} \left(\theta_{ij} - \theta_{ij}^{(0)} \right)^2, \quad (8)$$

where $k_B = 2 \times 10^{-19}$ N m [59] is the bending modulus; the sum runs over all the neighbouring triangular elements, and θ_{ij} is the angle between the normals of the i -th and j -th elements ($\theta_{ij}^{(0)}$ is the same angle in the unperturbed configuration). Once we have the total free-energy $W = W_S + W_B$, we compute the force acting on the i -th node by performing the derivative of W with respect to the coordinates of the node \mathbf{x}_i :

$$\mathbf{F}_i = -\frac{\partial W(\mathbf{x}_i)}{\partial \mathbf{x}_i}. \quad (9)$$

Note that we are implementing neither area nor volume conservation: in fact, as stated in [33], we checked that both area and volume were conserved, even without an

explicit area or volume conservation law (see Electronic Supplementary Material in [33]).

Regarding the viscoelastic term, we implemented the Standard Linear Solid (SLS) model [60, 36]. The viscous stress tensor is given by

$$\boldsymbol{\tau}^\nu = \mu_s (2\dot{\mathbf{E}} - \text{tr}(\dot{\mathbf{E}})\mathbf{1}) + \mu_d \text{tr}(\dot{\mathbf{E}})\mathbf{1}, \quad (10)$$

where \mathbf{E} is the strain tensor (see [60, 33]); μ_s and μ_d are the strain and dilation membrane viscosity: in this work, we assume $\mu_s = \mu_d = \mu_m$ [33]. We refer to [60, 33] for the computation of the stress tensor Eq. (10) as well as for the nodal force \mathbf{F}_i .

Finally, once we have the nodal force \mathbf{F}_i for each node i of the 3D mesh, we spread this force to the lattice nodes via the IBM (see [52] for details). We adopt the same scheme as in [33].

3 Loading and relaxation time

In this section, we quantitatively study the loading time t_L and the relaxation time t_R with three different loading mechanisms (see Fig. 1): the stretching with optical tweezers (STS, see Sec. 3.1), the deformation in simple shear flow (SHS, see Sec. 3.2) and the deformation in an elongational flow (FRMS, see Sec. 3.3). These three simulations differ mainly for two aspects (summarised in Tab. 1): the first one is that the membrane can be deformed by an external force which acts directly on the membrane (like in the STS) or by the viscous friction with the fluid (SHS and FRMS); moreover, the membrane can rotate (like in the SHS) or not (STS and FRMS). The idea underlying the choice of these three different setups is to catch which of the aforementioned characteristics affects the loading and relaxation dynamics.

In order to quantify the loading time t_L and the relaxation time t_R , we define the deformation parameter

$$D(t) = \frac{d_A(t) - d_T(t)}{d_A(t) + d_T(t)}, \quad (11)$$

where d_A and d_T represent the length of the axial and transversal diameters, i.e., the greater and medium eigenvalues of the inertia tensor (see [33]). In our computational domain, d_A and d_T lie in the $x - y$ plane. We define the average deformation D_{av} , i.e., the value of the deformation D such that $\lim_{t \rightarrow \infty} D(t) = D_{av}$ in the loading simulation and $D(0) = D_{av}$ in the relaxation simulation.

Qualitatively, the loading time t_L is the characteristic time the deformation $D(t)$ takes to reach D_{av} ; the relaxation time t_R is the characteristic time needed to relax to the initial shape, after the arrest of the mechanical load. Quantitatively, we can get t_L and t_R via a fit of $D(t)/D_{av}$ with the following functions:

$$L_1(t) = 1 - \exp \left\{ - \left(\frac{t}{t_L} \right)^\delta \right\}, \quad (12)$$

$$L_2(t) = 1 - \exp \left\{ - \left(\frac{t}{t_L} \right)^\delta \right\} \cos \left(\frac{t}{t_L^{\cos}} \right), \quad (13)$$

$$R(t) = \exp \left\{ - \left(\frac{t}{t_R} \right)^\delta \right\}, \quad (14)$$

where L_1 is used to fit the loading time for the STS and the FRMS (see Sec. 3.1-3.3, respectively); L_2 is used to fit the loading time for the SHS (see Sec. 3.2); R is used to fit the relaxation time t_R for all three simulations; δ is a parameter introduced to improve the fit [32] (see [33] for some more details).

Note that we propose two different functions to fit data during the loading (i.e. Eq. (12) and Eq. (13)); this is due to the different deformation process of the RBC: in the STS and FRMS, $D(t)$ is a monotonic increasing function with an asymptote in $D = D_{av}$ (see Fig. 1, panels (b) and (f)); in the SHS, $D(t)$ oscillates around D_{av} , and the amplitude of the oscillations varies with the value of the membrane viscosity μ_m (see Fig. 1, panel (d)). These oscillations have been also observed for viscoelastic capsules [38, 60, 33]. Since we want to compare the loading time t_L and the relaxation time t_R , we define the ratio

$$\tilde{t} = \frac{t_L}{t_R}. \quad (15)$$

In all the following simulations, the membrane viscosity ranges between $\mu_m \in [0, 3.18] \times 10^{-7}$ m Pa s [46, 18, 45, 47, 22, 48, 49, 17, 19, 32]. In the STS, the applied force is in the range $F \in [5, 90] \times 10^{-12}$ N; in the SHS, we simulated shear rates in the range $\dot{\gamma} \in [1.23, 123] \text{ s}^{-1}$; finally, in the FRMS, we simulated $F_{\text{roll}} \in [1, 120] \text{ s}^{-1}$ (see Eq. (16)).

3.1 Stretching simulation (STS)

In order to simulate the stretching with optical tweezers, we apply two forces with the same intensity F and opposite directions at the ends of the RBC (see Fig. 1, panel (a)). Simulations are performed in a 3D box $L_x \times L_y \times L_z = (28, 12, 12) \times 10^{-6}$ m. In Fig. 2, we report the loading time t_L (panel (a)) and the relaxation time t_R (panel (b)) as a function of F , for different values of membrane viscosity μ_m . In both cases, increasing the loading strength (as well as decreasing the value of membrane viscosity μ_m) results in a faster dynamics. It is interesting to compare t_L and t_R : in Fig. 2, panel (c), we report the ratio \tilde{t} (see Eq. (15)). As expected, decreasing the value of F , t_L and t_R tend to coincide; on the other hand, increasing F leads to a loading time t_L that is smaller than t_R .

3.2 Shear simulation (SHS)

In the shear simulation, the deformation is due to a linear shear flow with intensity $\dot{\gamma}$. We set the wall velocity $\mathbf{U}_w = (\pm \dot{\gamma}/2, 0, 0)$, and the RBC is oriented as reported in Fig. 1, panel (c): we chose this orientation to allow for a precise estimation of the loading and relaxation times: indeed, without such a choice one would meet complications coming from the emergence of other dynamical modes [61, 29]. Simulations are performed in a 3D box

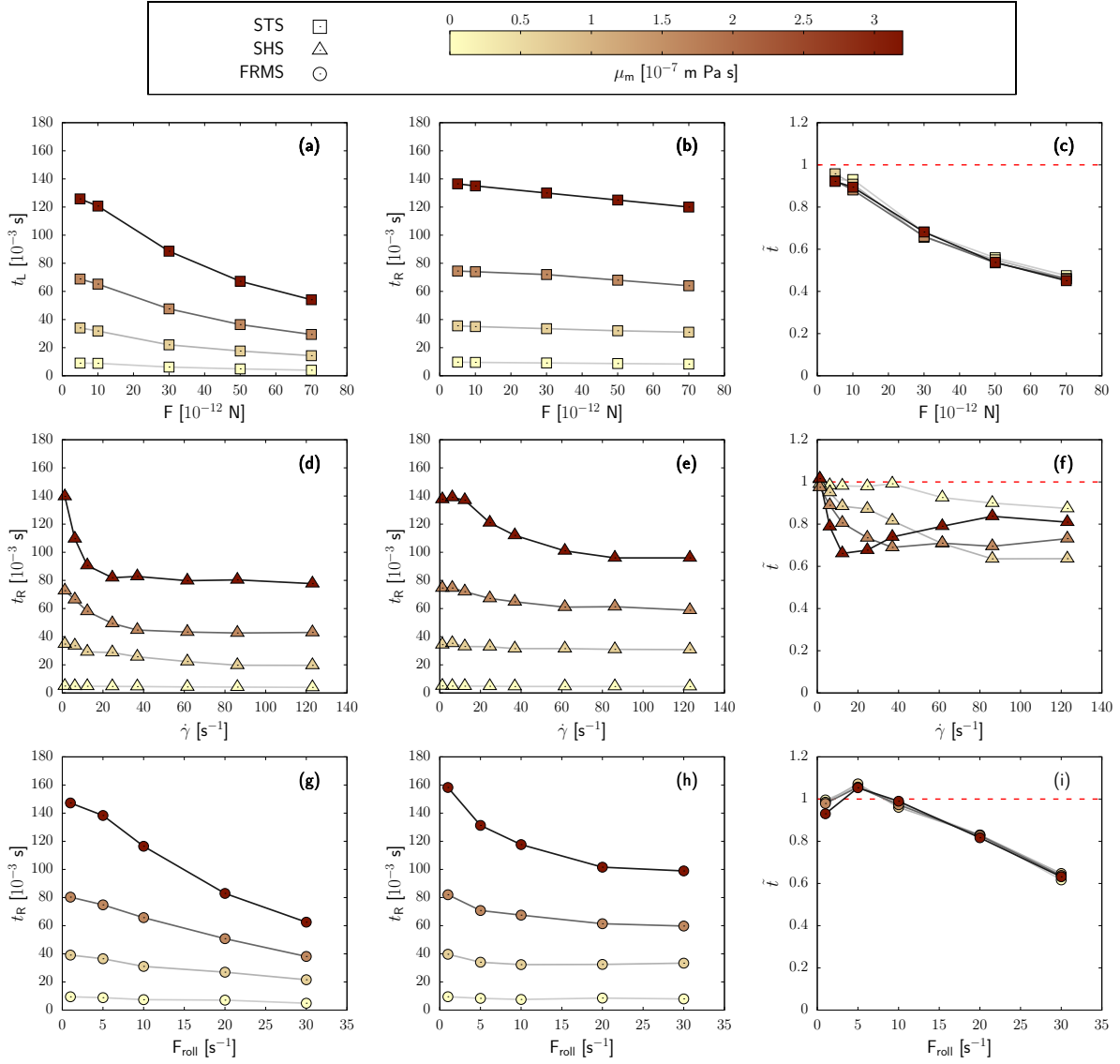


Figure 2: Characteristic times t_L (first column of panels) and t_R (second column of panels) as well as the ratio $\tilde{t} = t_L/t_R$ (third column of panels) are reported for the three simulations performed, i.e., stretching simulation (STS, \square , panels (a-c), Sec. 3.1), shear simulation (SHS, \triangle , panels (d-f), Sec. 3.2), four-roll mill simulation (FRMS, \circ , panels (g-i), Sec. 3.3), for different values of membrane viscosity μ_m (from lightest to darkest color): $\mu_m = 0.0 \text{ m Pa s}$ ($\square, \triangle, \circ$), $\mu_m = 0.64 \times 10^{-7} \text{ m Pa s}$ ($\square, \triangle, \circ$), $\mu_m = 1.59 \times 10^{-7} \text{ m Pa s}$ ($\square, \triangle, \circ$), $\mu_m = 3.18 \times 10^{-7} \text{ m Pa s}$ ($\blacksquare, \blacktriangle, \bullet$). The red dashed line represents the reference value for the symmetric case, i.e., $\tilde{t} = 1$.

$L_x \times L_y \times L_z = (20, 32, 20) \times 10^{-6} \text{ m}$. In Fig. 2, the loading time t_L (panel (d)) and the relaxation time t_R (panel (e)) as functions of $\dot{\gamma}$ for different values of membrane viscosity μ_m are reported, as well as the ratio \tilde{t} (panel (f)). While the relaxation time t_R shows a similar behaviour compared to the STS (see Fig. 2, panel (b)), a few more words are needed regarding the loading time t_L . Unlike the STS, now we have two characteristic times, that are t_L and t_L^{cos} (see Eq. (13)): t_L measures the time the membrane takes to reach the average deformation D_{av} , while t_L^{cos} measures the period of the oscillations. Data for t_L^{cos}

are reported in ESI†, Fig. 1. In contrast to the STS, the loading time t_L first decreases, and then it does not change much with the intensity of the mechanical load.

3.3 Four-roll mill simulation (FRMS)

In this case, we simulate the effect of four cylinders rotating [51], as shown in Fig. 1, panel (e), in order to create a flow similar to a pure elongational one. Simulations are performed in a 3D box $L_x \times L_y \times L_z = (48, 48, 20) \times 10^{-6} \text{ m}$. The idea is to simulate a loading mechanism that is a mix-

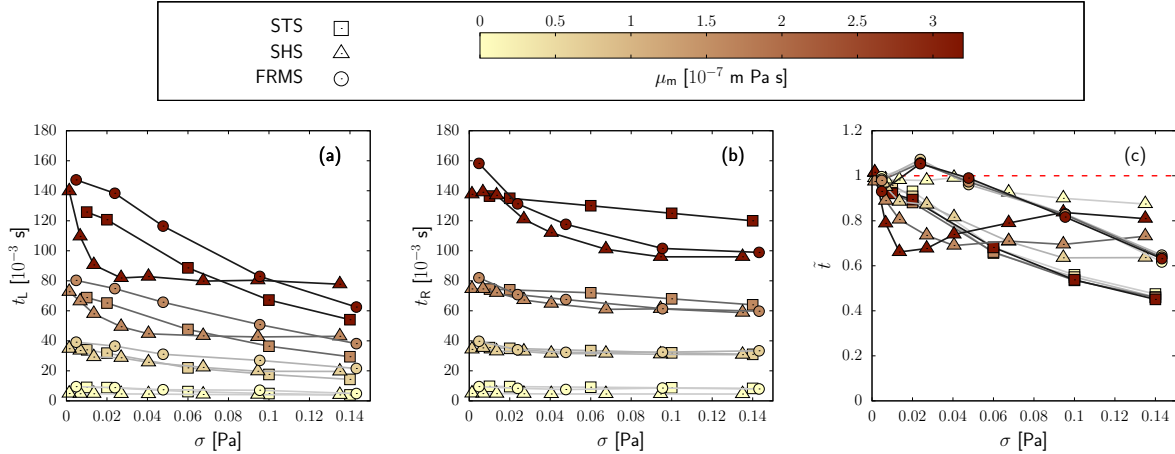


Figure 3: Comparison between the characteristic times t_L (panel (a)), t_R (panel (b)) and $\tilde{t} = t_L/t_R$ (panel (c)) as functions of the stress σ (see Sec. 4) for the three simulations performed, i.e., stretching simulation (STS, \square , Sec. 3.1), shear simulation (SHS, \triangle , Sec. 3.2), four-roll mill simulation (FRMS, \circ , Sec. 3.3), for different values of membrane viscosity μ_m (from lightest to darkest color): $\mu_m = 0.0 \text{ m Pa s}$ (\square , \triangle , \circ), $\mu_m = 0.64 \times 10^{-7} \text{ m Pa s}$ (\square , \triangle , \circ), $\mu_m = 1.59 \times 10^{-7} \text{ m Pa s}$ (\blacksquare , \blacktriangle , \bullet), $\mu_m = 3.18 \times 10^{-7} \text{ m Pa s}$ (\blacksquare , \blacktriangle , \bullet). The red dashed line represents the reference value for the symmetric case, i.e., $t = 1$.

ture of stretching with optical tweezers and deformation in simple shear flow (see Tab. 1): in fact, in this case, the membrane does not rotate (like in the STS) and the deformation is caused by the flow (like in the SHS).

To create such a flow, we impose a force density [51]

$$\mathbf{F}(x, y) = 2k\mu F_{\text{roll}} \begin{pmatrix} \sin(kx) \cos(ky) \\ -\cos(kx) \sin(ky) \\ 0 \end{pmatrix}, \quad (16)$$

where $k = 2\pi/L_x$, μ is the local fluid viscosity, and F_{roll} is used to tune the load strength. We multiplied Eq. (16) by k to make the velocity gradient independent of the size of the fluid domain*:

$$\frac{\partial \mathbf{u}}{\partial \mathbf{x}} = F_{\text{roll}} \begin{pmatrix} \cos(kx) \cos(ky) & -\sin(kx) \sin(ky) \\ \sin(kx) \sin(ky) & -\cos(kx) \cos(ky) \end{pmatrix}, \quad (17)$$

where we have reported the only x and y components, i.e., the components in the plane of the shear. Note that Eq. (16) gives a pure elongational flow only in $x = \pi/2, 3\pi/2$ and in $y = \pi/2, 3\pi/2$.

In Fig. 2 we report the loading time t_L (panel (g)) and the relaxation time t_R (panel (h)) as a function of F_{roll} . As for the STS and the SHS, both t_L and t_R decrease when the loading force increases or the membrane viscosity μ_m decreases. In Fig. 2, panel (i), the ratio \tilde{t} is reported.

4 Discussion

In our simulations, the intensity of the three mechanical loads is changed by varying different quantities, i.e., F for

the STS, $\dot{\gamma}$ for the SHS and F_{roll} for the FRMS. To facilitate a comparison between them, we first consider the characteristic times t_L and t_R as well as the ratio \tilde{t} as functions of the characteristic simulation stress σ (Fig. 3). To evaluate the stress σ for the STS, we computed the area A at the end of the RBC where the force F is applied. Then, the stress is given by $\sigma^{\text{STS}} = F/A$; for the SHS, we wrote the stress as $\sigma^{\text{SHS}} = 2\dot{\gamma}/\mu_{\text{out}}$. Finally, for the FRMS, the stress is given by the stress-peak $\sigma^{\text{FRMS}} = \mu_{\text{out}}F_{\text{roll}}$. In all three simulations, the loading and relaxation times (t_L and t_R , respectively) show qualitatively the same behaviour, i.e., they decrease when the loading strength increases or when the membrane viscosity μ_m decreases (see Fig. 3, panels (a) and (b)); the ratio $\tilde{t} = t_L/t_R$ is reported in Fig. 3, panel (c). For small forces ($\sigma \rightarrow 0$) we observe a clear tendency towards *symmetry* between loading and relaxation ($\tilde{t}(\sigma, \mu_m) \rightarrow 1$), meaning that the characteristic times t_L and t_R tend to be equal. This is the limit where one expects to recover the *intrinsic* dynamics of the membrane, which depends only on the value of membrane viscosity μ_m [33, 19].

On the other hand, for finite force strengths, loading and relaxation dynamics are *asymmetrical*, i.e., $\tilde{t} \neq 1$ for $\sigma \neq 0$. As already noticed elsewhere [42], this asymmetry could be explained by energetic considerations: in fact, during the loading phase, the deformation is driven by the external load (i.e., an external source of energy), while during the relaxation, the membrane provides the whole energy. Beyond these qualitative considerations, results in Fig. 3 provide a systematic characterization of the relaxation times, as a function of either the stress σ or the membrane viscosity μ_m : an important message conveyed by our analysis is that the *asymmetry is not universal*, i.e., on equal values of membrane viscosity μ_m , the ratio \tilde{t} depends on the kind of

* The following result is valid in a homogeneous fluid with dynamics viscosity μ .

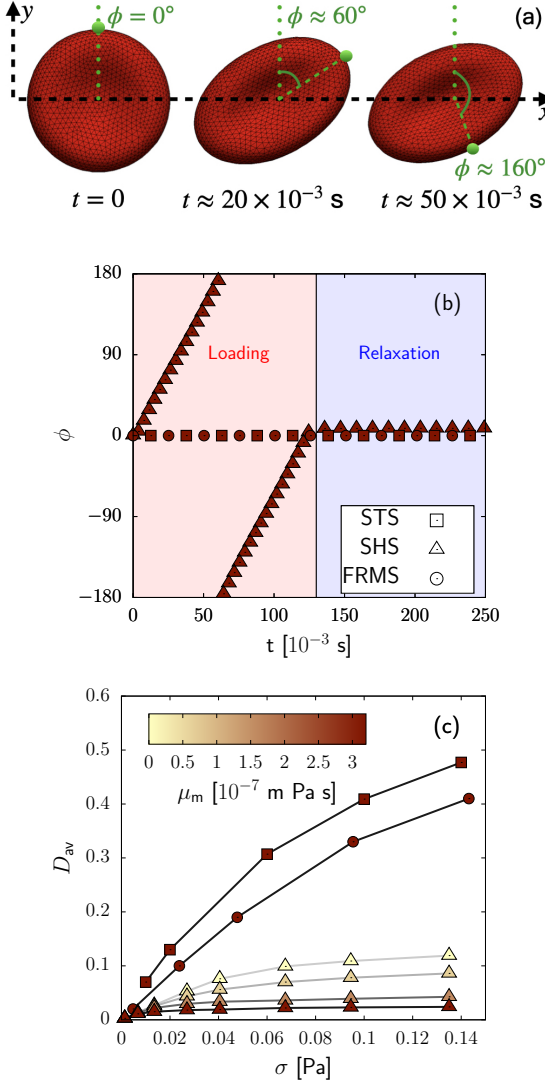


Figure 4: *Panel (a)*: snapshots of RBC at selected times. A point is selected on the membrane (green sphere) to perform a Lagrangian tracking and determine the time dependency of the angle ϕ that the point direction forms with the y axis in the deformation plane. *Panel (b)*: we report the angle ϕ (see panel (a) above) as a function of time for the stretching simulation (STS, \square , Sec. 3.1), shear simulation (SHS, \triangle , Sec. 3.2), four-roll mill simulation (FRMS, \circ , Sec. 3.3), for $\mu_m = 3.18 \times 10^{-7} \text{ m Pa s}$. The red and blue shades represent loading and relaxation regions, respectively. *Panel (c)*: average deformation D_{av} (see text for details) as a function of the stress σ for the three simulations performed (STS, SHS and FRMS). SHS data are displayed for different values of membrane viscosity μ_m (from lightest to darkest color): $\mu_m = 0.0 \text{ m Pa s}$ (\triangle), $\mu_m = 0.64 \times 10^{-7} \text{ m Pa s}$ (\triangle), $\mu_m = 1.59 \times 10^{-7} \text{ m Pa s}$ (\blacktriangle), $\mu_m = 3.18 \times 10^{-7} \text{ m Pa s}$ (\blacktriangledown). STS data (\blacksquare) and FRMS data (\bullet) data are only reported for $\mu_m = 3.18 \times 10^{-7} \text{ m Pa s}$.

mechanical load. Just to give some numbers, the difference between the values of \tilde{t} for the STS and FRMS is roughly constant ($\approx 30\%$) and it goes to zero for small values of σ ; for the SHS the situation is a bit more complex because \tilde{t} depends on μ_m . However, if we compare SHS against STS for $\mu_m = 3.18 \times 10^{-7} \text{ m Pa s}$, we find a difference of less than 30% for small values of σ (i.e., $\sigma < 0.1 \text{ Pa}$), while such a difference goes over the 50% for large values of σ (i.e., $\sigma > 0.1 \text{ Pa}$).

If we think that the asymmetry comes from the presence of a mechanical load with finite strength [43, 42], it comes naturally to expect a non-universality and a dependency on the details of the loading mechanism. Thanks to our analysis, we are in a condition to further characterise this non-universality: indeed, we observe that while \tilde{t} does not depend on μ_m for the STS and FRMS ($\tilde{t}^{STS} = \tilde{t}^{STS}(\sigma)$, $\tilde{t}^{FRMS} = \tilde{t}^{FRMS}(\sigma)$), it actually does in the SHS ($\tilde{t}^{SHS} = \tilde{t}^{SHS}(\sigma, \mu_m)$). The collapse shown by \tilde{t} in the STS and FRMS (see Fig. 3, panel (c)) suggests a factorisation of the loading and relaxation times in two contributions: one depending on the membrane viscosity μ_m and one on the load intensity σ :

$$\tilde{t}_L^K(\sigma, \mu_m) \approx t_L^{*K}(\sigma) t_0^K(\mu_m) \quad \text{for } K = \text{STS, FRMS} , \quad (18)$$

$$\tilde{t}_R^K(\sigma, \mu_m) \approx t_R^{*K}(\sigma) t_0^K(\mu_m) \quad \text{for } K = \text{STS, FRMS} , \quad (19)$$

where the superscript K stands for the kind of mechanical load. Given this factorisation, we have

$$\tilde{t}^K(\sigma) = \frac{t_L^{*K}(\sigma)}{t_R^{*K}(\sigma)} \quad \text{for } K = \text{STS, FRMS} . \quad (20)$$

To make progress, we investigated what is the physical ingredient at the core of the factorization given in Eqs. (18)-(19), or, alternatively, why the SHS does not factorize as in Eqs. (18)-(19). We argue that such a difference between SHS and STS/FRMS is mainly due to the different dynamics that are induced by the mechanical load. First of all, as already stated in Sec. 3, in the SHS there are two characteristic times in the loading process (see Eq. (13)), one related to the time the deformation takes to reach the steady value D_{av} , and one related to the period of the oscillation (t_L and t_L^{\cos} , respectively). The main difference between SHS and STS/FRMS lies in the rotation of the membrane (see Tab. 1) that is present only in the SHS. In fact, one can split the velocity gradient $\frac{\partial \mathbf{u}}{\partial \mathbf{x}}$ in the symmetric (rotational) and antisymmetric (elongational) parts:

$$\frac{\partial \mathbf{u}}{\partial \mathbf{x}} = \begin{pmatrix} 0 & \dot{\gamma} \\ 0 & 0 \end{pmatrix} = \begin{pmatrix} 0 & \dot{\gamma} \\ \dot{\gamma} & 0 \end{pmatrix} + \begin{pmatrix} 0 & \dot{\gamma} \\ -\dot{\gamma} & 0 \end{pmatrix} , \quad (21)$$

where the only two components in the shear plane are reported. The rotational part causes the rolling motion of the membrane (see Fig. 4, panels (a) and (b)), while the elongational one tends to deform the RBC and pushes the main diameter to an angle of $\pi/4$ with respect to the shear direction; an increase in the membrane viscosity causes an increase in the time needed for the membrane to adapt to the flow and to deform; meanwhile, the rotational

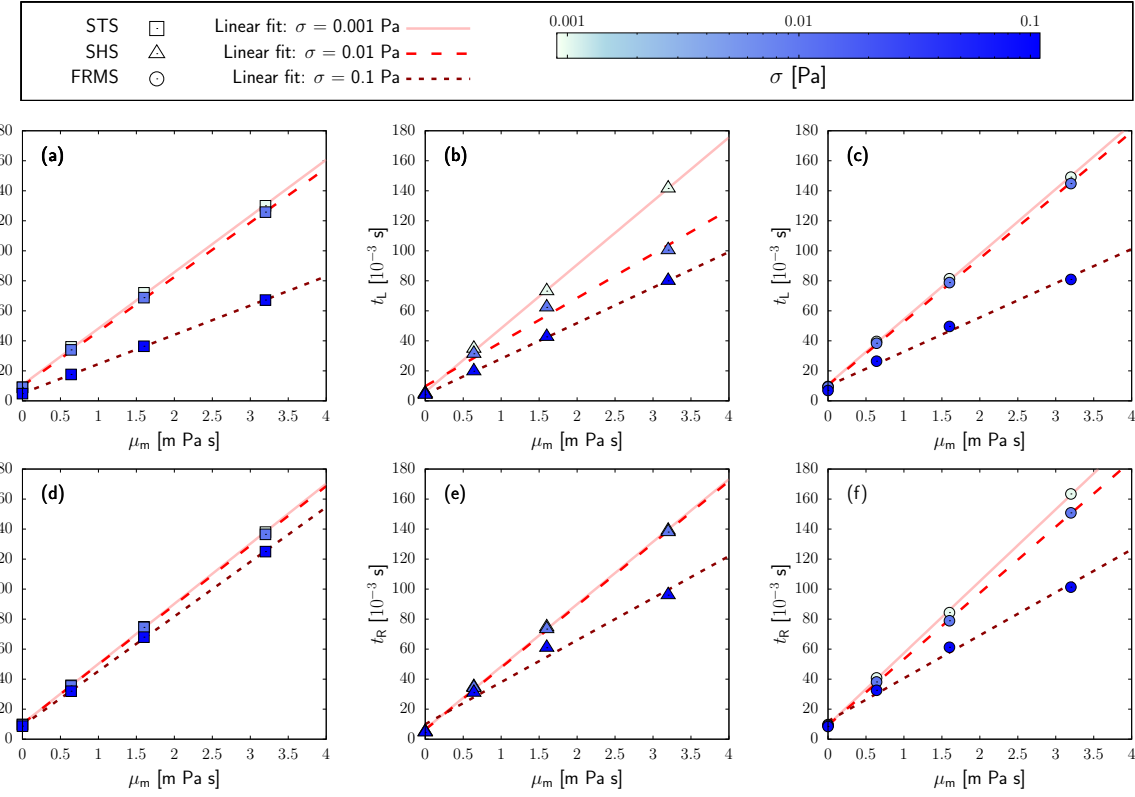


Figure 5: Characteristic times t_L (panels (a-c)) and t_R (panels (d-f)) as functions of the membrane viscosity μ_m (see Sec. 4) for the three performed simulations: stretching simulation (STS, \square , Sec. 3.1), shear simulation (SHS, \triangle , Sec. 3.2), four-roll mill simulation (FRMS, \circ , Sec. 3.3), for different values of stress σ (from lightest to darkest color): $\sigma = 0.001$ Pa ($\square, \triangle, \circ$), $\sigma = 0.01$ Pa ($\blacksquare, \blacktriangle, \bullet$), $\sigma = 0.1$ Pa ($\blacksquare, \blacktriangle, \bullet$).

component promotes a rotation of the main diameter. Overall, the increase in membrane viscosity μ_m leads to a decrease of the average deformation D_{av} (see also Fig. 4, panel (c)). To make these arguments clearer, we have made two videos available in the Ancillary File†: in one we show the simulation with $\dot{\gamma} = 1.23$ s $^{-1}$ and $\mu_m = 3.18 \times 10^{-7}$ m Pa s, while in the other one the simulation with $\dot{\gamma} = 1.23$ s $^{-1}$ and $\mu_m = 0$ m Pa s is reported. In both cases, the tank-treading motion of the membrane appears, but, for $\mu_m = 0$ m Pa s, the membrane deforms more than in the case with $\mu_m = 3.18 \times 10^{-7}$ m Pa s. In Fig. 4, panel (c), we report the average deformation D_{av} as a function of the stress σ for all three mechanical loads at changing the membrane viscosity μ_m . Since D_{av} is not sensitive to the value of membrane viscosity μ_m for the STS and FRMS, for these two cases we report only points for $\mu_m = 3.18 \times 10^{-7}$ m Pa s. It emerges that, in the SHS, the average deformation D_{av} saturates at a constant value: an increase in the shear rate $\dot{\gamma}$ causes an initial increase of the average deformation D_{av} ; then, D_{av} reaches a plateau and increasing the shear rate $\dot{\gamma}$ beyond a certain value does not result in an increased deformation. The higher the membrane viscosity μ_m , the lower is the value of $\dot{\gamma}$ for which the plateau is reached. Furthermore,

when compared to the STS and FRMS, we can see that on the same values of σ the average deformation D_{av} is much smaller in the SHS. Again, this is due to the rotation of the membrane during the loading. In both STS and FRMS, the membrane does not rotate, so that the energy injected by the flow is used to deform the membrane. These investigations reveal that it is impossible to predict the loading and relaxation times if we only know the deformation and have no information about the kind of mechanical load.

In view of the above considerations on the deformation, it appears also natural to study the characteristic times as functions of the average deformation D_{av} . We performed this analysis (see ESI†, Fig. 2), confirming the picture displayed in Fig. 3: again, \tilde{t} shows a collapse for the STS and the FRMS and does not depend on the value of the membrane viscosity μ_m ; for the SHS \tilde{t} shows a dependency on both D_{av} and the membrane viscosity μ_m . The results on $t_L(D_{av})$ and $t_R(D_{av})$ (Fig. 2 in ESI†, panels (a) and (b), respectively) further confirm that in general there is no correlation between the degree of deformation of the membrane and the characteristic times for different kinds of mechanical loads.

In our previous work [33], we have already seen that, for

small forces, t_R is linear in μ_m , in agreement with literature predictions [19]. Now we can go further, and we study the dependency of both t_L and t_R as functions of μ_m for different values of σ . This will help further to determine to what degree these two kinds of dynamics can be regarded as different dynamics [43, 42]. In Fig. 5, we report both $t_L(\mu_m)$ and $t_R(\mu_m)$ (first and second row of panels, respectively) for three values of σ spanning two orders of magnitude as well as their linear fit (whose coefficients are reported in ESI†, Tab. 1) for all three simulations (STS in panel (a) and (d); SHS in panel (b) and (e); FRMS in panel (c) and (f)). In all three simulations, for a fixed value of σ , the linear approximation is reasonably good. For small values of σ (e.g., $\sigma = 0.001$ Pa), both t_L and t_R are similar for all three simulations; that is not surprising, since at small values of stress σ the intrinsic properties of the membrane arise. Regarding the sensitivity of the linear trend with respect to a change in σ , we observe different behaviours in the two dynamics. Regarding the loading dynamics, we observe that for high values of σ , the three load mechanisms provide similar linear fits, while in the intermediate region of σ , the SHS shows a different behaviour with respect to the STS and FRMS. Regarding the relaxation dynamics, the variability of the linear trends with the value of the stress is more pronounced in presence of hydrodynamical forces (i.e. SHS and FRMS), while in the STS the linear behaviour of t_R with respect to μ_m is only slightly perturbed by a change in the stress if compared to the others. These quantitative observations are summarized in Tab. 1 in ESI†.

Before concluding this section, a few words must be said about the parameter δ used to improve the fit (see Eqs. (12)-(13)-(14)): in general, in all three setups, δ is close to one, especially in the STS and FRMS (see Fig. 3 loading in the SHS, where the parameter δ seems to tend asymptotically to $\delta \approx 0.6$ at increasing values of shear rate $\dot{\gamma}$: this deviation from 1 reflects the effect of the kind of mechanical load also on δ , showing that, during the loading in the SHS, $D(t)$ is not that close to an exponential function, and multiple loading times arise [33].

5 Conclusions

A comprehensive characterisation of the viscoelastic properties of the RBC membrane, as well as the way the membrane responds to an external force, are crucial information in different fields, from the detection of pathologies [11, 16, 19], to the design of biomedical devices [24, 25, 26, 27]. Having a more quantitative information on the time-dependent response of the RBC membrane at varying the intensity and the typology of the mechanical load is a key ingredient in designing some biomedical devices. One example comes from the VADs [62]: if the residence time inside the impeller (that is the region where the RBCs experience a wide range of stress) is much shorter than the loading time, RBCs do not have time to deform; on the contrary, a higher residence time leads to a

finite deformation that can cause hemolysis. When an external force acts on a viscoelastic membrane, two main kinds of dynamics arise: the *loading* and the *relaxation* dynamics with associated times t_L and t_R . Earlier investigations pointed to the fact that these two kinds of dynamics are two distinct processes, since during the relaxation there is no external force to drive the membrane, in contrast to the loading [43, 42]. To the best of our knowledge, however, an exhaustive comparative characterization of these two kinds of dynamics has never been conducted. This motivated our work to investigate these two kinds of dynamics with different setups that involve different typologies of mechanical loads (whose main features are summarised in Tab. 1) while performing a parametric study on the values of membrane viscosity μ_m . The latter choice is motivated by the large variability of membrane viscosity values reported in the literature [46, 18, 45, 47, 22, 48, 49, 17, 19, 32].

The two kinds of dynamics are *symmetrical* ($\tilde{t} = t_L/t_R \rightarrow 1$) in the limit of small load strengths ($\sigma \rightarrow 1$), i.e., in the limit where the response function of the RBC is dominated by the "intrinsic" properties of the membrane; in marked contrast, we found an *asymmetry* in the two kinds of dynamics for finite load strengths ($\tilde{t} = t_L/t_R \neq 1$ for $\sigma > 0$), meaning that the loading dynamics is always faster than the relaxation one. We found that the asymmetry profoundly depends on the kind of mechanical load and we have demonstrated this non-universality via a quantitative study in terms of the applied load strength σ and the value of membrane viscosity μ_m . There are some realistic load mechanisms, like shear flows, that make the membrane rotate during loading, while leaving the membrane relaxing to the shape at rest without rotation: in this case, the contribution that the membrane viscosity gives to the characteristic times t_L and t_R differs, and then the ratio \tilde{t} is a function of both the stress σ and the membrane viscosity μ_m . From the other side, there are other realistic load mechanisms, like the stretching with optical tweezers or the deformation with an elongational flow, in which the membrane deforms without rotating during both processes. In this case, the contribution given by the membrane viscosity μ_m to the characteristic times is the same during both loading and relaxation, and as a consequence, the ratio \tilde{t} is a function of the stress σ only. Finally, even though we showed that both loading and relaxation dynamics are not universal, we found that for a given value of the stress σ , a linear increase of the characteristic times as functions of the membrane viscosity μ_m is a fair approximation in all cases.

We argue our findings offer interesting physical and practical insights on the response function and the unsteady dynamics of RBCs driven by realistic mechanical loads.

Conflicts of interest

There are no conflicts to declare.

Acknowledgements

The authors acknowledge L. Biferale and G. Koutsou. This project has received funding from the European Union Horizon 2020 Research and Innovation Program under the Marie Skłodowska-Curie grant agreement No. 765048. We also acknowledge support from the project “Detailed Simulation of Red blood Cell Dynamics accounting for membRane viscoElastic propertieS” (SorCeReS, CUP No. E84I19002470005) financed by the University of Rome “Tor Vergata” (“Beyond Borders 2019” call).

References

- [1] A. S. Popel and P. C. Johnson, *Annu. Rev. Fluid Mech.*, 2005, **37**, 43–69.
- [2] R. Skalak and P. Branemark, *Science*, 1969, **164**, 717–719.
- [3] T. Krüger, *Computer simulation study of collective phenomena in dense suspensions of red blood cells under shear*, Springer Science & Business Media, 2012.
- [4] L. Mountrakis, *Transport of blood cells studied with fully resolved models*, 9789462597754, 2015.
- [5] F. Janoschek, *Mesoscopic simulation of blood and general suspensions in flow*, Technische Universiteit Eindhoven, 2013.
- [6] M. Gross, T. Krüger and F. Varnik, *Soft Matter*, 2014, **10**, 4360–4372.
- [7] T. Krüger, M. Gross, D. Raabe and F. Varnik, *Soft Matter*, 2013, **9**, 9008–9015.
- [8] D. A. Fedosov, B. Caswell and G. E. Karniadakis, *Biophysical journal*, 2010, **98**, 2215–2225.
- [9] W. Pan, D. A. Fedosov, B. Caswell and G. E. Karniadakis, *Microvascular research*, 2011, **82**, 163–170.
- [10] D. A. Fedosov, B. Caswell and G. E. Karniadakis, *Computer Methods in Applied Mechanics and Engineering*, 2010, **199**, 1937–1948.
- [11] T. Krüger, D. Holmes and P. V. Coveney, *Biomicrofluidics*, 2014, **8**, 054114.
- [12] D. A. Fedosov, W. Pan, B. Caswell, G. Gompper and G. E. Karniadakis, *Proceedings of the National Academy of Sciences*, 2011, **108**, 11772–11777.
- [13] A. Guckenberger, A. Kihm, T. John, C. Wagner and S. Gekle, *Soft Matter*, 2018, **14**, 2032–2043.
- [14] D. A. Fedosov, H. Noguchi and G. Gompper, *Biomechanics and modeling in mechanobiology*, 2014, **13**, 239–258.
- [15] J. Mills, L. Qie, M. Dao, C. Lim and S. Suresh, *MCB-TECH SCIENCE PRESS*, 2004, **1**, 169–180.
- [16] S. Suresh, J. Spatz, J. P. Mills, A. Micoulet, M. Dao, C. Lim, M. Beil and T. Seufferlein, *Acta biomaterialia*, 2005, **1**, 15–30.
- [17] S. Braunmüller, L. Schmid, E. Sackmann and T. Franke, *Soft Matter*, 2012, **8**, 11240–11248.
- [18] S. Chien, K. L. Sung, R. Skalak, S. Usami and A. Tözeren, *Biophysical Journal*, 1978, **24**, 463–487.
- [19] G. Prado, A. Farutin, C. Misbah and L. Bureau, *Biophysical Journal*, 2015, **108**, 2126–2136.
- [20] S. Hénon, G. Lenormand, A. Richert and F. Gallet, *Biophysical Journal*, 1999, **76**, 1145 – 1151.
- [21] R. Hochmuth, P. Worthy and E. Evans, *Biophysical journal*, 1979, **26**, 101–14.
- [22] O. Baskurt and H. Meiselman, *Biorheology*, 1996, **33**, 489 – 503.
- [23] P. Bronkhorst, G. Streekstra, J. Grimbergen, E. Nijhof, J. Sixma and G. Brakenhoff, *Biophysical journal*, 1995, **69**, 1666–1673.
- [24] T. Murakami, L. R. Golding, G. B. Jacobs, S. Takatani, R. Sukalac, H. Harasaki and Y. NONE, *Jinko Zoki*, 1979, **8**, 636–639.
- [25] K. Nonaka, J. Linneweber, S. Ichikawa, M. Yoshikawa, S. Kawahito, M. Mikami, T. Motomura, H. Ishitoya, I. Nishimura, D. Oestmann et al., *Artificial Organs*, 2001, **25**, 675–682.
- [26] M. Behbahani, M. Behr, M. Hormes, U. Steinseifer, D. Arora, O. Coronado and M. Pasquali, *European Journal of Applied Mathematics*, 2009, **20**, 363–397.
- [27] D. Arora, M. Behr and M. Pasquali, *Artificial organs*, 2006, **30**, 539–547.
- [28] Q. Zhu and R. J. Asaro, *Physics of Fluids*, 2019, **31**, 051901.
- [29] D. Cordasco and P. Bagchi, *Physics of Fluids*, 2017, **29**, 041901.
- [30] D. Cordasco and P. Bagchi, *Journal of Fluid Mechanics*, 2016, **800**, 484.
- [31] D. Cordasco and P. Bagchi, *Journal of Fluid Mechanics*, 2014, **759**, 472.
- [32] D. A. Fedosov, *Multiscale modeling of blood flow and soft matter*, Brown University, 2010.
- [33] F. Guglietta, M. Behr, L. Biferale, G. Falcucci and M. Sbragaglia, *Soft Matter*, 2020, **16**, 6191–6205.
- [34] F. Guglietta, M. Behr, L. Biferale, G. Falcucci and M. Sbragaglia, *arXiv preprint arXiv:2012.06190*, 2020.
- [35] M. Dao, C. T. Lim and S. Suresh, *Journal of the Mechanics and Physics of Solids*, 2003, **51**, 2259–2280.
- [36] P. Li and J. Zhang, *Biomechanics and Modeling in Mechanobiology*, 2020, 1–15.
- [37] P. Li and J. Zhang, *Cardiovascular Engineering and Technology*, 2021.
- [38] A. Yazdani and P. Bagchi, *Journal of Fluid Mechanics*, 2013, **718**, 569–595.

[39] K. Graessel, C. Bächer and S. Gekle, *Journal of Fluid Mechanics*, 2021, **910**, A46.

[40] H. Noguchi and G. Gompper, *Physical Review E*, 2005, **72**, 011901.

[41] H. Noguchi and G. Gompper, *Physical review letters*, 2007, **98**, 128103.

[42] D. Barthes-Biesel, *Annual Review of fluid mechanics*, 2016, **48**, 25–52.

[43] A. Diaz, N. Pelekasis and D. Barthes-Biesel, *Physics of Fluids*, 2000, **12**, 948–957.

[44] E. A. Evans, *Methods in enzymology*, Elsevier, 1989, vol. 173, pp. 3–35.

[45] R. M. Hochmuth, P. Worthy and E. A. Evans, *Biophysical journal*, 1979, **26**, 101–114.

[46] E. Evans and R. Hochmuth, *Biophysical journal*, 1976, **16**, 1–11.

[47] R. Tran-Son-Tay, S. Sutera and P. Rao, *Biophysical journal*, 1984, **46**, 65–72.

[48] B. D. Riquelme, J. R. Valverde and R. J. Rasia, *Optical Diagnostics of Biological Fluids V*, 2000, pp. 132–140.

[49] G. Tomaiauolo and S. Guido, *Microvascular research*, 2011, **82**, 35–41.

[50] S. R. Keller and R. Skalak, *Journal of Fluid Mechanics*, 1982, **120**, 27–47.

[51] O. Malaspinas, N. Fiétier and M. Deville, *Journal of Non-Newtonian Fluid Mechanics*, 2010, **165**, 1637–1653.

[52] T. Krüger, H. Kusumaatmaja, A. Kuzmin, O. Shardt, G. Silva and E. M. Viggen, *The Lattice Boltzmann Method - Principles and Practice*, 2016.

[53] S. Succi, *The lattice Boltzmann equation: for fluid dynamics and beyond*, Oxford university press, 2001.

[54] Z. Guo, C. Zheng and B. Shi, *Phys. Rev. E*, 2002, **65**, 046308.

[55] S. Frijters, T. Krüger and J. Harting, *Computer Physics Communications*, 2015, **189**, 92 – 98.

[56] E. Evans and Y.-C. Fung, *Microvascular research*, 1972, **4**, 335–347.

[57] R. Skalak, A. Tozeren, R. P. Zarda and S. Chien, *Biophysical journal*, 1973, **13**, 245–264.

[58] W. Helfrich, *Zeitschrift fur Naturforschung. Teil C: Biochemie, Biophysik, Biologie, Virologie*, 1973, **28**, 693–703.

[59] G. Gompper and M. Schick, *Soft Matter: Lipid Bilayers and Red Blood Cells*, Wiley-VCH, 2008.

[60] P. Li and J. Zhang, *International Journal for Numerical Methods in Biomedical Engineering*, 2019, **35**, e3200.

[61] C. Minetti, V. Audemar, T. Podgorski and G. Coupier, *Journal of fluid mechanics*, 2019, **864**, 408–448.

[62] S. Haßler, A. M. Ranno and M. Behr, *Computer Methods in Applied Mechanics and Engineering*, 2020, **369**, 113171.

ELECTRONIC SUPPLEMENTARY INFORMATION FOR: LOADING AND RELAXATION DYNAMICS OF A RED BLOOD CELL

Fabio Guglietta

Department of Physics & INFN, *University of Rome “Tor Vergata”*^{*}

Chair for Computational Analysis of Technical Systems (CATS), *RWTH Aachen University*[†]

Computation-based Science and Technology Research Center, *The Cyprus Institute*[‡]

fabio.guglietta@roma2.infn.it

Marek Behr

Chair for Computational Analysis of Technical Systems (CATS), *RWTH Aachen University*[†]

Giacomo Falcucci

Department of Enterprise Engineering “Mario Lucertini,” *University of Rome “Tor Vergata”*[§]

Mauro Sbragaglia

Department of Physics & INFN, *University of Rome “Tor Vergata”*^{*}

^{*}Via della Ricerca Scientifica 1, 00133, Rome, Italy

[†]52056 Aachen, Germany

[‡]20 Konstantinou Kavafi Str., 2121 Nicosia, Cyprus

[§]Via del Politecnico 1, 00133, Rome, Italy

1 Shear simulation (SHS): characteristic time t_L^{\cos}

In Fig. 1, values of t_L^{\cos} are reported (see Eq. (13) in main paper) as a function of the shear rate $\dot{\gamma}$ for different values of membrane viscosity μ_m . While t_L measures the time the membrane takes to reach the average deformation D_{av} , the characteristic time t_L^{\cos} measures the period of the oscillations.

2 Characteristic times as functions of the average deformation

In Fig. 2 we report the characteristic times t_L and t_R (see Eqs. (12)-(14) in main paper) as well as the ratio $\tilde{t} = t_L/t_R$ as function of the average deformation D_{av} .

3 δ parameter

In Fig. 3 we report the values of the parameter δ used to interpolate t_L , t_L^{\cos} and t_R (see Eqs. (12)-(14) in main paper).

4 Movies

Four movies showing the loading-relaxation simulations for all three kinds of mechanical loads simulated are available in the Ancillary Files:

- STS: stretching simulation with $F = 50 \times 10^{-12}$ N and $\mu_m = 3.18 \times 10^{-7}$ m Pa s (see Sec. 3.1 in main paper).
- SHS: shear simulation with $\dot{\gamma} = 123$ s $^{-1}$ and $\mu_m = 3.18 \times 10^{-7}$ m Pa s (see Sec. 3.2 in main paper).
- SHS_mum0: shear simulation with $\dot{\gamma} = 123$ s $^{-1}$ and $\mu_m = 0.0$ m Pa s (see Sec. 3.2 in main paper).
- FRMS: four-roll mill simulation with $F_{roll} = 10$ s $^{-1}$ and $\mu_m = 3.18 \times 10^{-7}$ m Pa s (see Sec. 3.3 in main paper).

5 Supplementary figures

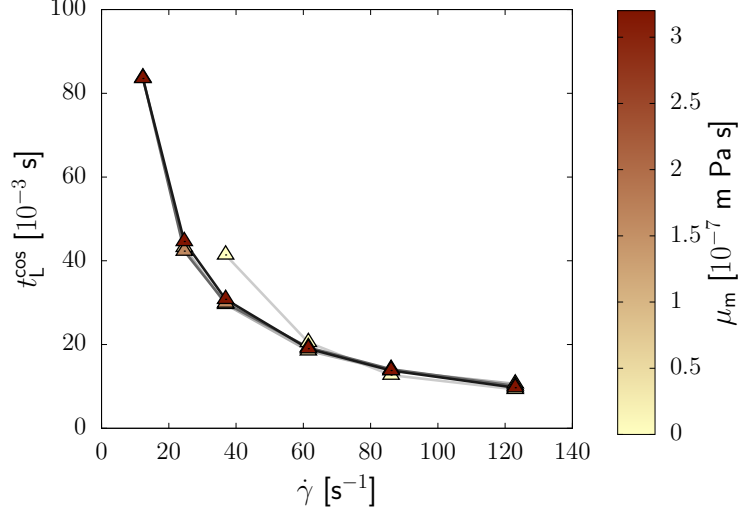


Figure 1: Values of t_L^{\cos} as a function of the shear rate $\dot{\gamma}$ (see Eq. (13) in main paper) for different values of membrane viscosity μ_m (from lightest to darkest color): $\mu_m = 0.0 \text{ m Pa s}$ (\triangle), $\mu_m = 0.64 \times 10^{-7} \text{ m Pa s}$ (\triangle), $\mu_m = 1.59 \times 10^{-7} \text{ m Pa s}$ (\blacktriangle), $\mu_m = 3.18 \times 10^{-7} \text{ m Pa s}$ (\blacktriangle).

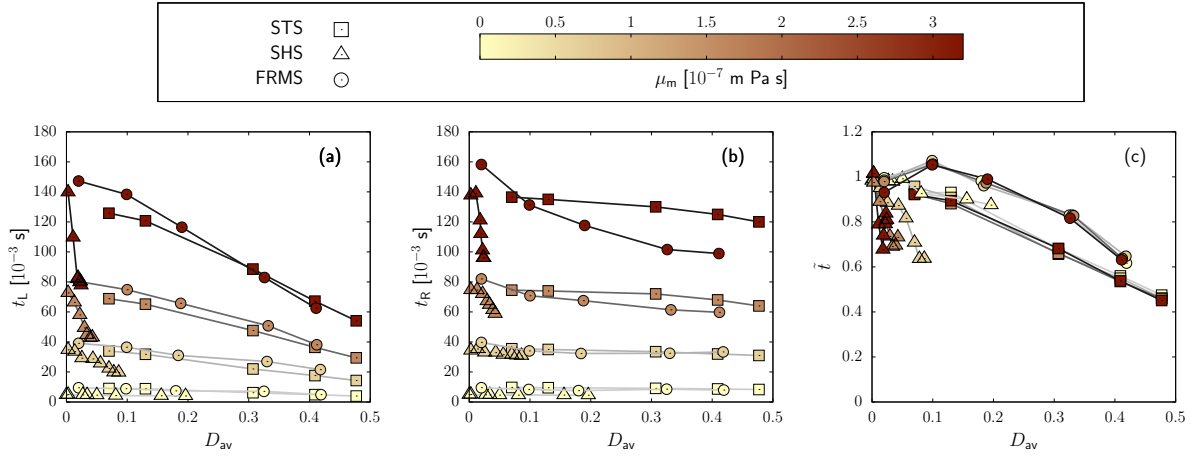


Figure 2: Comparison between the characteristic times t_L (panel (a)), t_R (panel (b)) and the ratio $\tilde{t} = t_L/t_R$ (panel (c)) as functions of the average deformation D_{av} (see Sec. 4 in main paper) for the three simulations performed, i.e., stretching simulation (STS, \square), shear simulation (SHS, \triangle), four-roll mill simulation (FRMS, \circ), for different values of membrane viscosity μ_m (from lightest to darkest color): $\mu_m = 0.0 \text{ m Pa s}$ (\square , \triangle , \circ), $\mu_m = 0.64 \times 10^{-7} \text{ m Pa s}$ (\square , \triangle , \circ), $\mu_m = 1.59 \times 10^{-7} \text{ m Pa s}$ (\blacksquare , \blacktriangle , \bullet), $\mu_m = 3.18 \times 10^{-7} \text{ m Pa s}$ (\blacksquare , \blacktriangle , \bullet).

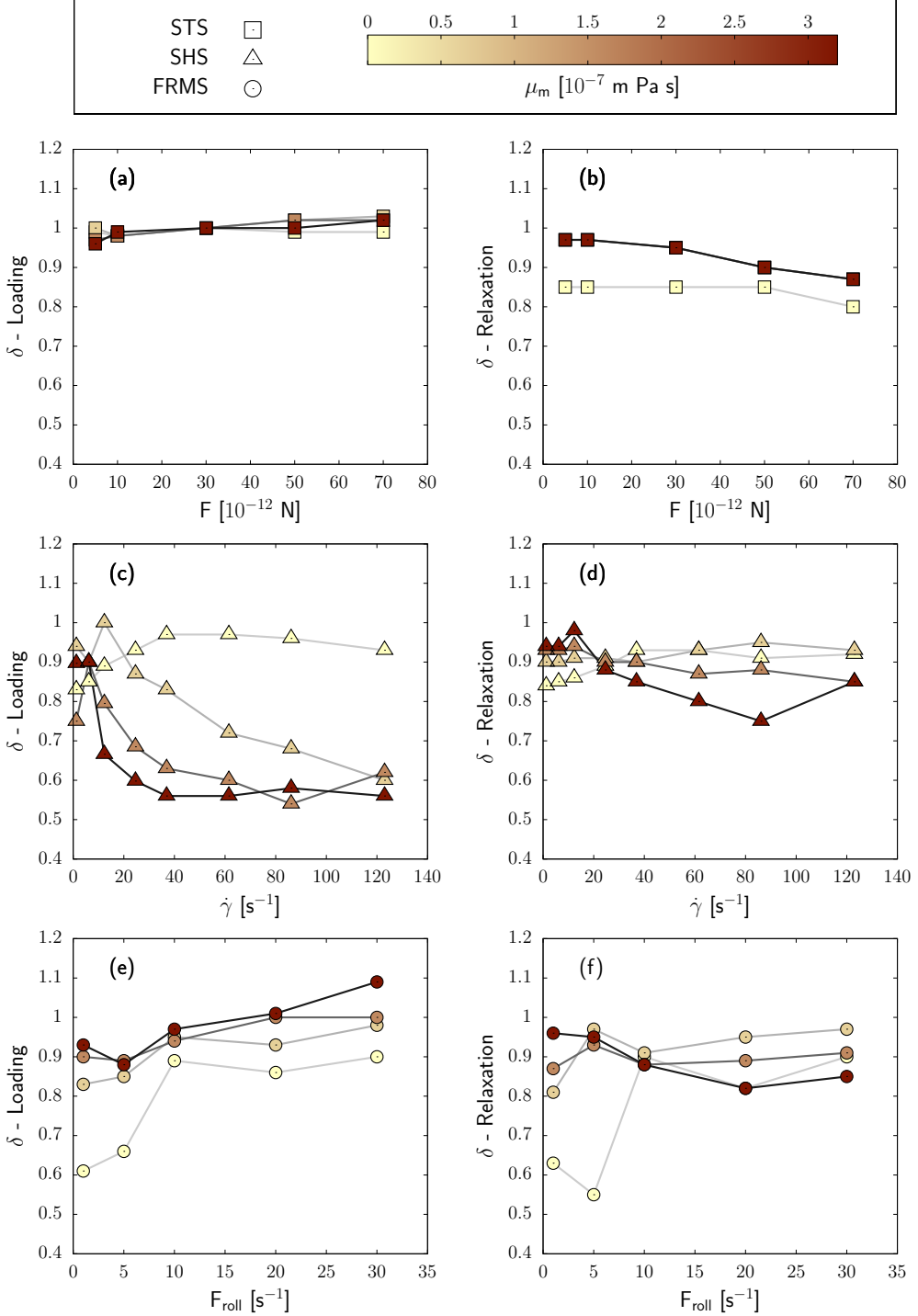


Figure 3: Values of the parameter δ used to interpolate t_L , t_L^{\cos} and t_R (see Eqs. (12)-(14) in main paper) are reported for the three simulations performed, i.e., stretching simulation (STS, \square , panels (a-c), Sec. 3.1), shear simulation (SHS, \triangle , panels (d-f), Sec. 3.2), four-roll mill simulation (FRMS, \circ , panels (g-i), Sec. 3.3), for different values of membrane viscosity μ_m (from lightest to darkest color): $\mu_m = 0.0 \text{ m Pa s}$ (\square , \triangle , \circ), $\mu_m = 0.64 \times 10^{-7} \text{ m Pa s}$ (\blacksquare , \blacktriangle , \bullet), $\mu_m = 1.59 \times 10^{-7} \text{ m Pa s}$ (\blacksquare , \blacktriangle , \bullet).

6 Supplementary tables

		STS		SHS		FRMS	
		L	R	L	R	L	R
$\sigma = 0.001 \text{ Pa}$	a	10.7 ± 1.3	10.2 ± 0.4	5.9 ± 1.1	6.7 ± 1.5	10.9 ± 1.1	9.4 ± 1.1
	b	37.5 ± 0.7	40.0 ± 0.2	42.4 ± 0.6	41.6 ± 0.8	43.4 ± 0.6	47.9 ± 0.6
$\sigma = 0.01 \text{ Pa}$	a	9.9 ± 0.8	10.2 ± 0.6	9.8 ± 4.6	6.3 ± 1.4	10.5 ± 1.0	9.2 ± 0.6
	b	36.3 ± 0.4	39.6 ± 0.3	29.4 ± 2.5	41.4 ± 0.7	42.2 ± 0.5	44.1 ± 0.3
$\sigma = 0.025 \text{ Pa}$	a	8.8 ± 0.2	9.9 ± 0.8	9.4 ± 4.0	7.3 ± 2.0	9.8 ± 0.8	9.0 ± 0.6
	b	33.8 ± 0.1	39.1 ± 0.4	23.8 ± 2.0	34.6 ± 1.1	40.0 ± 0.5	38.0 ± 0.4
$\sigma = 0.05 \text{ Pa}$	a	6.8 ± 0.2	9.8 ± 1.0	6.6 ± 2.2	8.1 ± 3.0	8.9 ± 1.7	9.7 ± 2.2
	b	28.1 ± 0.1	38.1 ± 0.6	23.6 ± 1.0	33.3 ± 1.7	33.4 ± 0.9	33.9 ± 1.2
$\sigma = 0.075 \text{ Pa}$	a	5.6 ± 0.2	9.4 ± 0.8	5.4 ± 0.9	9.6 ± 4.0	9.6 ± 2.3	10.9 ± 2.6
	b	23.4 ± 0.1	37.3 ± 0.5	23.4 ± 0.5	29.1 ± 2.0	27.9 ± 1.2	31.0 ± 1.5
$\sigma = 0.1 \text{ Pa}$	a	5.0 ± 0.2	8.9 ± 0.5	4.4 ± 0.3	10.0 ± 5.0	10.0 ± 2.7	12.0 ± 3.1
	b	19.5 ± 0.1	36.4 ± 0.3	23.7 ± 0.2	28.0 ± 3.0	22.8 ± 1.5	28.6 ± 1.7
$\sigma = 0.125 \text{ Pa}$	a	4.5 ± 0.2	8.6 ± 0.2	4.6 ± 0.7	9.6 ± 4.5	8.7 ± 2.6	12.1 ± 3.4
	b	17.0 ± 0.1	35.4 ± 0.1	23.2 ± 0.4	27.9 ± 2.4	19.7 ± 1.4	28.1 ± 1.8

Table 1: Coefficients a_L , a_R , b_L and b_R used to fit $t_L(\mu_m)$ and $t_R(\mu_m)$ for the STS, SHS and FRMS at some fixed value of the stress σ . We use linear fits, $t_L^{\text{FIT}} = a_L + b_L \mu_m$ and $t_R^{\text{FIT}} = a_R + b_R \mu_m$, respectively (see Fig. 5 in main paper). Values of a are expressed in $[10^{-3} \text{ s}]$, while values of b are expressed in $[10^4 \text{ m}^{-1} \text{ Pa}^{-1}]$.